Journal of Magnetic Resonance 198 (2009) 88–93

Contents lists available at ScienceDirect

Journal of Magnetic Resonance

journal homepage: www.elsevier.com/locate/jmr

Visualization of inhomogeneous local magnetic field gradient due to susceptibility contrast

H. Cho [a,b], S. Ryu [b], J.L. Ackerman [c], Y.-Q. Song [b,*]

[a] Memorial Sloan Kettering Cancer Center, 1275 York Avenue, New York, NY 10021, USA
[b] Schlumberger-Doll Research, One Hampshire Street, Cambridge, MA 02139, USA
[c] The Athinoula A. Martinos Center for Biomedical Imaging, Massachusetts General Hospital, 149 13th street, Charlestown, MA 02129, USA

ARTICLE INFO

Article history:
Received 24 June 2008
Revised 20 January 2009
Available online 23 February 2009

Keywords:
Internal magnetic field
Background gradient
Porous media

ABSTRACT

We visualized inhomogeneous local magnetic field (internal magnetic field) gradients arising from susceptibility contrast between an array of cylindrical glass tubes (solid matrix) and surrounding water (pore fluids) in a uniform applied magnetic field. MRI was performed to determine the spatially resolved decay rates due to diffusion in the internal magnetic field which were proportional to the strength of local gradient. We also spatially resolved the interference pattern of the cross-terms between the internal and the applied field gradient in order to extract the orientation of the internal field gradient. These experimental results were found to be consistent with the theoretical calculations. This work demonstrates a simple yet representative case for visualizing the strength and orientation of the local susceptibility induced magnetic field gradients in porous media.

1. Introduction

Nuclear magnetic resonance (NMR) has been widely used as a non-destructive way to characterize porous media. Pore space properties, such as porosity, permeability and surface-to-volume ratio, can be determined via spin relaxation measurements [1–3], time-dependent diffusion coefficient $D(t)$, and diffusion propagator measurements [4–8].

When a porous material is placed in a uniform magnetic field, spatially varying fields ($\vec{B}^{\text{int}}(r)$) typically arise inside the pore space due to susceptibility contrasts ($\triangle\chi$) between the solid matrix and the surrounding fluid. Susceptibility contrast is present in many porous media of interest, such as fluid filled rocks, cements, granular media, colloids and trabecular bones. The presence of non-uniform internal fields often interferes with NMR relaxation and diffusion measurements. Much effort has gone into understanding the effect of the internal gradient (also called background gradient) on NMR response and designing pulse sequences to cope with its interference with the applied gradient [9–11,5,12–14]. Recently, the idea of utilizing internal gradients as a finger-print of pore geometry has been proposed and implemented in the laboratory [15–17].

Historically, Brown et al. first computed magnetic field distributions from a single magnetized grain and a random packing of grains and observed the effects of such distributions on the decay of NMR signals [18]. Detailed numerical evaluation of the internal field in a 2D pack of cylinders and 3D random pack of spheres has been reported [19,20]. NMR responses were numerically evaluated based on CT images for sandstone and carbonate rocks [21].

Susceptibility-induced contrast (T_2^*) in biologic systems is often used to obtain functional and structural information of underlying tissues, as in the BOLD effect [22] in functional MRI applications and the characterization of trabecular bone structure [23,24]. Hwang et al. applied MR phase mapping techniques to measure internal magnetic field in trabecular bone and showed good agreement with theoretical calculations based on surface charge method [23]. Sigmund et al. showed that DDIF contrast [15] from bone/fluid interface is sensitive to the projected surface to volume ratio of trabecular bone [24]. On the other hand, susceptibility induced magnetic field gradients are vector quantities, and the ability to obtain not only the strength/phase but the orientation information with MR method may provide unique opportunities to study the morphology of underlying tissues in more quantitative details. For example, T_2^* in lung tissue tends to be very short [25] and to exhibit a distribution of values [26] because of the air–tissue interface. Characterizing and understanding direction-dependent susceptibility effects could lead to improved lung imaging methods, as well as providing information on the microstructure of lung tissue [27]. Furthermore, capillary blood vessel geometry is known to be a significant determinant of susceptibility contrasts [28]. The ability to measure the directional dependence of susceptibility contrast in capillaries will provide useful information in quantifying microvascular tortuosity in tumor angiogenesis or in determining the preferential capillary direction in myocardial walls [29].

* Corresponding author. Fax: +1 617 768 2386.
E-mail address: ysong@slb.com (Y.-Q. Song).

1090-7807/$ - see front matter © 2009 Elsevier Inc. All rights reserved.
doi:10.1016/j.jmr.2009.01.024

In this paper, we utilized the decay of the magnetization due to spins diffusing in the internal magnetic field (DDIF) for the direct experimental visualization of the strength of internal gradients. We performed microimaging experiments on a vessel-mimicking phantom composed of uniform cylindrical capillary tubes. Interference patterns of the cross-terms between the internal and applied gradient were resolved along different pulsed field gradient (PFG) orientations permitting the extraction of the vector components of the internal gradient and thus allowing directional mapping of internal gradients. Excellent agreement with theoretical calculations was observed.

2. Method

The sample consisted of an array of glass capillary tubes (Fisherbrand) with an ID 1.15 mm and wall thickness 0.2 mm, packed into a 13-mm NMR tube. It was filled with water both inside and between capillaries. MRI experiments were performed in a horizontal 4.7-T magnet (Bruker Biospin, Billerica, MA) with a 30-G/cm gradient set and a homemade RF probe tuned to 200 MHz. The orientation of the applied field was along the y direction which was perpendicular to the cylindrical axis (z) of the glass tubes. The internal field gradient is only in x–y plane due to the symmetry of the sample and the field direction.

A slice-selective stimulated echo sequence with spin-warp imaging was employed, shown in Fig. 1. The two t_e periods function as the encoding and decoding periods of the internal field gradient and t_d was the diffusion time. The duration (t_p) of the slice selective $\pi/2$ pulse was 2 ms and the strength of the slice gradient (G_s) was 4 G/cm. Transverse spin magnetization after the first $\pi/2$ pulse develops a spatially dependent phase due to the internal gradients. At the end of the encoding period, the encoded transverse magnetization was flipped back into the longitudinal direction and the spins diffuse during the t_d period. The third $\pi/2$ pulse was applied to produce a stimulated echo for magnetization detection and imaging. The decay of the echo was measured at a series of t_d values. The effective decay rates of the echo signal can be written as

$$\frac{1}{T_{\text{eff}}} = \frac{1}{T_1} + \frac{1}{T_{\text{ext}}} + \frac{1}{T_{\text{int}}} = \frac{1}{T_b} + \gamma^2 t_e^2 D g_{\text{int}}^2, \tag{1}$$

where γ, D and g_{int} are the gyromagnetic ratio, diffusion constant and the internal field gradient, respectively. $1/T_{\text{ext}} = \gamma^2 D(t_p G_s/2)^2$ originates from the unbalanced slice gradient during the second RF pulse and can be estimated to be 0.3 s^{-1}. Bulk relaxation

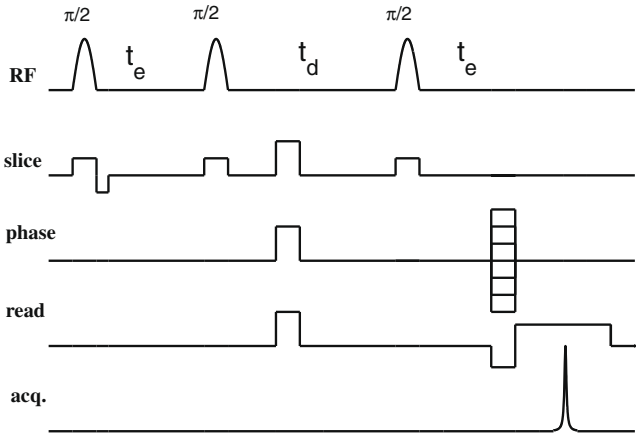

Fig. 1. Slice selective 2D spin-warp stimulated echo imaging sequence for DDIF contrast. The spoiler gradients were applied during t_d to remove unwanted coherence pathway signals other than the stimulated echo.

T_1 ($\sim 0.4\ s^{-1}$) also contributes to the effective signal decay. Therefore, there exists a total background decay rate $1/T_b$ of $\sim 0.7\ s^{-1}$ in addition to the decay due to internal field gradients ($1/T_{\text{int}}$).

The encoding time (t_e) was 0.040 s and the diffusion time (t_d) was varied from 0.05 to 1.1 s. Imaging was performed with a 2-mm slice thickness and the image matrix size was 256×256 with an in-plane resolution of 51 μm. The signal decay as a function of t_d was fitted to a single exponential function for individual pixels of the image and background rates ($1/T_b$) were subtracted to obtain the spatial map of DDIF decay rates. No adjustment was made for the signal free-region outside the NMR tube. The noise level was estimated from the signal-free region and only points whose amplitudes were larger than the noise level were included in the fits. All decay curves were found to be consistent with single exponential behavior within experimental error.

To probe the interference pattern between the internal and applied field gradients ($\vec{g} = \vec{g}_{\text{ext}} + \vec{g}_{\text{int}}$), a gradient pulse of 0.5 G/cm, similar to the value of internal field gradient, was applied for 35 ms during the encoding time (t_e) periods along three different orientations (read (B_0): y, phase: x, slice: z). The corresponding decay rate was proportional to the square of the local gradient:

$$g_i^2 = g_{\text{ext}}^2 + g_{\text{int}}^2 + 2\vec{g}_{\text{ext}} \cdot \vec{g}_{\text{int}}, \tag{2}$$

where $i = 1, 2, 3$ represents three experiments with different directions of applied gradient pulses. For example, the first experiment ($i = 1$) used the PFG along the z-direction, the second experiment along y and third along x, as shown in, Fig. 4. Since the internal field gradient is only in the x–y plane due to the cylindrical symmetry of the sample, the following relations hold

$$g_1^2 = g_z^2 + g_{\text{int}}^2, \tag{3}$$

$$g_2^2 = g_y^2 + g_{\text{int}}^2 + 2\vec{g}_y \cdot \vec{g}_{\text{int}}, \tag{4}$$

$$g_3^2 = g_x^2 + g_{\text{int}}^2 + 2\vec{g}_x \cdot \vec{g}_{\text{int}}, \tag{5}$$

since the magnitude of the applied gradients was the same, the cross-terms $\vec{g}_{\text{ext}} \cdot \vec{g}_{\text{int}}$ could be obtained by subtracting g_1^2 from g_2^2 and g_3^2. In addition, the contributions from bulk T_1 and unbalanced slice gradients were removed by this subtraction. Again, single exponential fitting was performed to obtain the decay rates of individual voxels, and thus the strength of the total gradients was determined from the spatially resolved interference pattern.

The numerical calculation of the internal field was performed as follows. First, a black and white representation (1024×1024 voxels) of cylinders was created from the measured spin density image at $t_d = 50$ ms to obtain a high resolution replica of the experimental setup. To minimize the boundary effect, the image was placed at the center of a 2048×2048 area. The induced (demagnetization) field along the external field direction was calculated in the Fourier space by superposition of the dipole field from each voxel of the solid taken as a point source, valid to first order in $\triangle\chi/\chi \ll 1$ [30,31]. From this, we obtained the strength of the gradient via $g_{\text{int}} = \sqrt{(dB_y/dy)^2 + (dB_y/dx)^2}$ as well as the angle-resolved gradient $\vec{g}_{\text{int}} \cdot \hat{n}$ ($\hat{n}$ is the unit vector along the direction of applied external gradient) evaluated on the grid.

3. Experimental results and discussion

Fig. 2 shows the images at four diffusion times. Distinct decay behaviors are apparent depending on the local packing geometry. Representative packings, such as rectangular, triangular and pentagonal, are illustrated in (d) for comparison. For example, signal decay is always slower at the centers of the local packing geometry where local minima in the internal fields (and therefore minimal gradients) tend to occur. The gradual thickening of the apparent capillary walls indicates higher gradients near the walls. Such

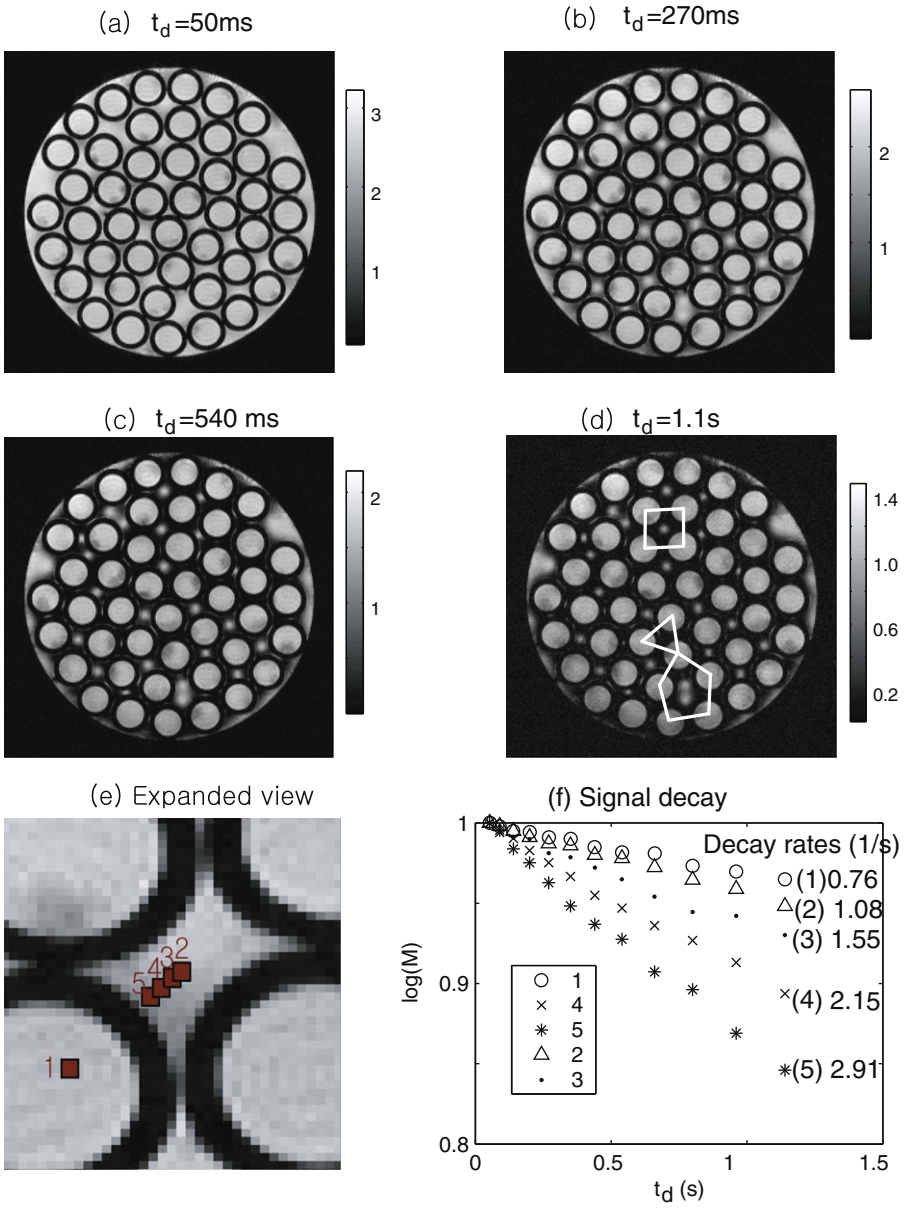

Fig. 2. Axial images with different diffusion times (t_d: 0.05 s (a), 0.27 s (b), 0.54 s (c) and 1.1 s (d)) show the spatially varying decay profiles across the pores. Several local packing geometries are highlighted in (d). (e) Shows a close-up of (a) and (f) plots the signal decay at the individual voxels denoted in (e).

behavior is demonstrated in panel (f) showing mono-exponential decays of representative voxels as labeled in the close-up panel (e). The observed mono-exponential decay is likely due to the imaging voxel size (0.05 mm) being small relative to the average pore sizes (0.5 mm) of capillary tubes and also because only initial decay was measured.

Fig. 3A and B show maps of the measured decay rates and those of the squares of the calculated internal field gradients, respectively. Panels (C) and (D) compare the experimental and theoretical values across several pores for various packing conditions along the labeled lines in (A) and (B). For comparison, the theoretical gradient value was multiplied by a factor in order to make it comparable to the experimental decay rate for the plots. The normalization factor was determined by comparing the average value of internal gradients strength in pores of triangular packing between calculated and experimental values. Overall agreement is excellent. Uniform decay inside the cylindrical tubes was observed. For rectangular packing, slow decay (weak internal gradient) in the symmetric center of the pore between the tubes were apparent and decay rates gradually increased toward the wall of the capillary tubes. For triangular packing, fast and uniform decay were observed in the pore. For pentagonal packing, double minima of decay rates stand out. The observed behaviors are consistent with the theoretical calculations of internal fields in the pores surrounded by regularly packed cylinders (rectangular packing) by Sen and Axelrod [19].

Experimental results are in good agreement with the numerical calculation of the internal field for the interior of the capillary tubes, as illustrated in Fig. 3C and D. For example, C1 and D1 both show a dip in the middle of the pore and increase close to the pore wall. C3 and D3 show a relatively constant gradient/decay across the pore. The finite resolution and the noise in the image that created the mask for the numerical calculation is likely to be responsible for the slight quantitative difference between the experiments and the calculation, such as the depth of the valleys in C4 and D4.

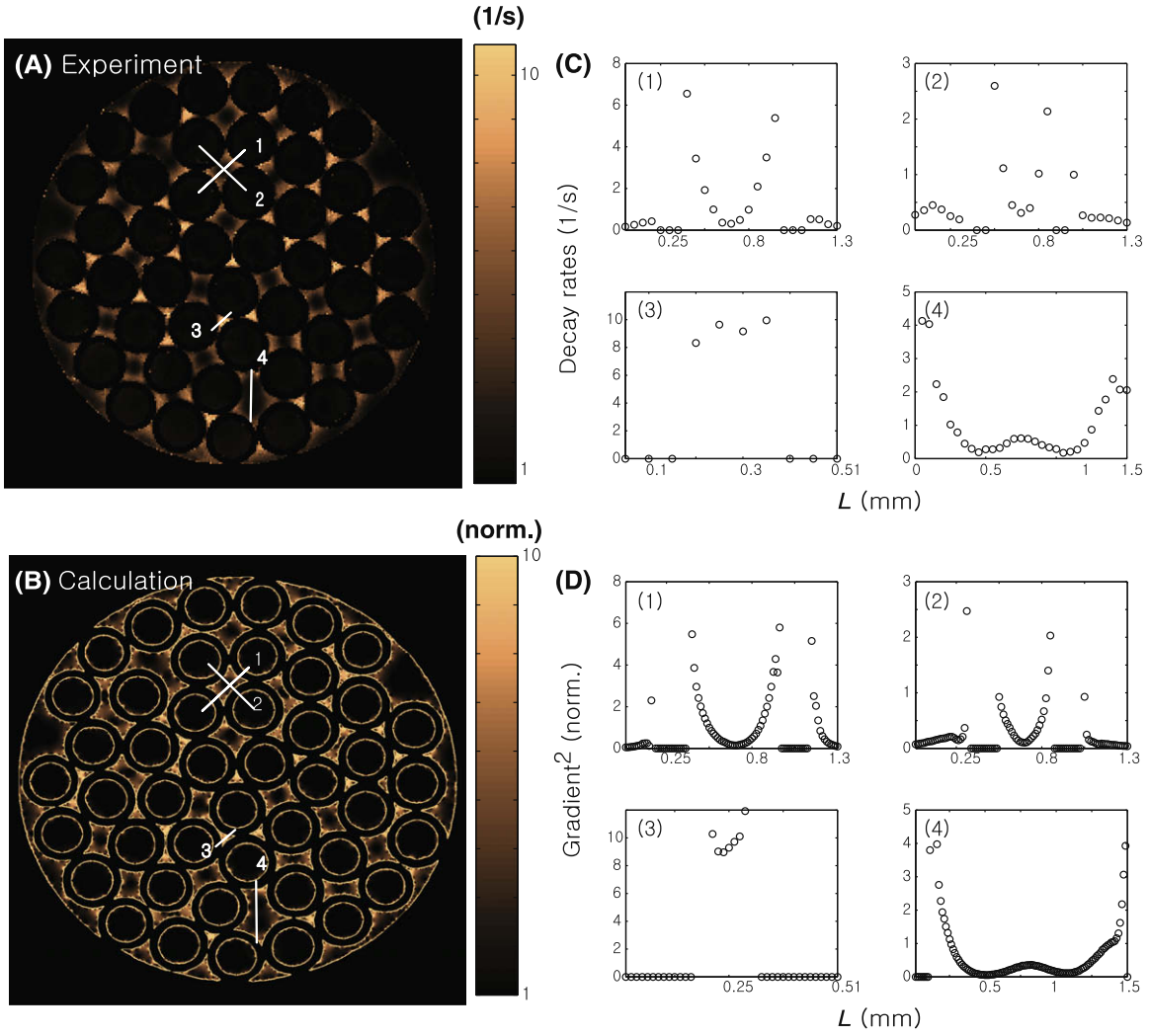

Fig. 3. (A) shows DDIF decay rates obtained from the imaging experiment and (B) shows the strength of the local gradient from the theoretical calculation. (C) Plots measured decay rates across the pores for various packing configurations along the labeled crossing lines in (A), and (D) shows corresponding gradient strength for comparison in (1 and 2) rectangular, (3) triangular, and (4) pentagonal packings. L is the coordinate along the lines. For comparison, the theoretical gradient value was multiplied by a factor in order to make it comparable to the experimental decay rate for the plots.

On the other hand, the numerical results show a pronounced gradient near the grain–pore interface from inside the cylinders (Fig. 3B), while the experimental gradient was low and flat. From the symmetry of the cylinder, we did not expect a significant gradient on the inside of the cylinders. This was because the contribution from the enclosing cylinder should be zero and the gradient is only due to nearby cylinders. However, in a numerical calculation, the cylinders were digitized on a cartesian grid so that the boundaries of the cylinders are not smooth, thus creating artificial zig-zag features on the surfaces of the cylinders. Such features produce field gradients over a length scale comparable to the width of the feature, i.e. the size of the voxels. Such imperfection in the modeling of the cylinder is the source of the error in the gradient calculation very near the cylinder surfaces.

Fig. 4 shows three maps of decay rates when the external field gradient was applied along different directions during the encoding period t_e. In (A), (B) and (C), the applied field gradient was 0.5 G/cm during the t_e period along the slice $(\otimes, z)$, read $(\uparrow, y)$, and phase $(\rightarrow, x)$ directions, respectively, and the refocusing gradient was applied during the decoding period. Interference patterns of decay rates between internal and external gradients were apparent, showing constructive interference on one side and destructive interference on the other side of each pore depending on the PFG directions. No interference along the slice direction was observed due to the cylindrical symmetry of the model system.

Using the measurements of Fig. 4, we extracted the decay rates due to cross-terms between internal and external gradients, shown in Fig. 5, and compared these decay rates to the corresponding theoretical calculations of angle-resolved internal gradients $(\vec{g}_{\text{int}} \cdot \hat{n})$. The sole contribution of cross-terms to the measured decay rates in the presence of both internal and external gradients was extracted by subtracting the decay rate map obtained with the PFG in the slice direction from the corresponding decay rate map with other PFG orientations. Fig. 4A was subtracted from either (B) or (C), with the resulting images in Fig. 5A and B.

Fig. 5A and B show experimental decay rates of cross-terms, where arrows represent the direction of applied PFG. Fig. 5C and D show theoretically calculated maps of the angle-resolved internal gradients along the respective directions. For rectangular packing, the direction of the internal gradients flips across the pore, which was not the case for triangular packing. In pentagonal packing, stronger internal gradients were observed close to the walls of the tubes without distinctive symmetry. The bottom panels of Fig. 5 quantitatively compare the strengths of experimentally measured cross-terms and theoretically calculated angle-resolved internal gradient across rectangular packing (A1 and C1) and trian-

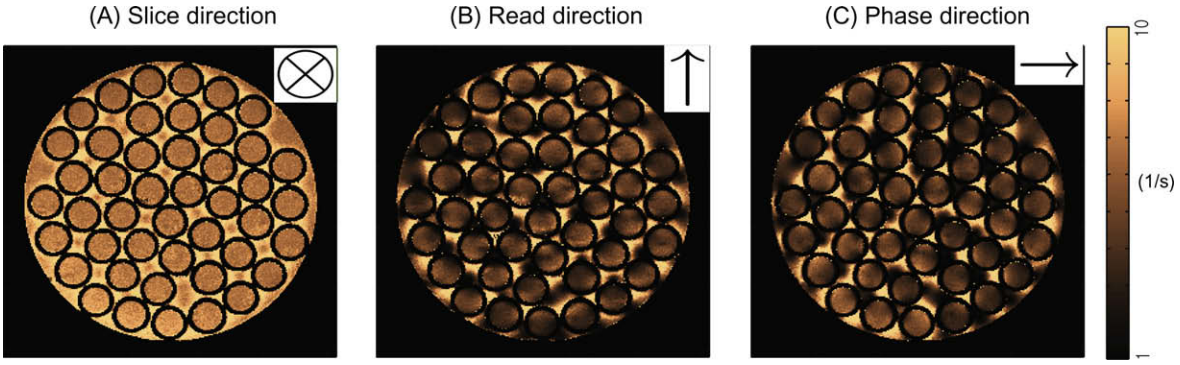

Fig. 4. Maps of decay rates when external field gradients were applied along different directions during the encoding period. Interference patterns were apparent. In (A), (B) and (C), the applied field gradient was along the slice (⊗), read (↑), and phase (→) directions, respectively. Notice the different patterns in B and C, and that both B and C, with gradients transverse to the tube axis, are very different from A, with gradient parallel to the tube axis. These differences allowed the extraction of the cross-terms.

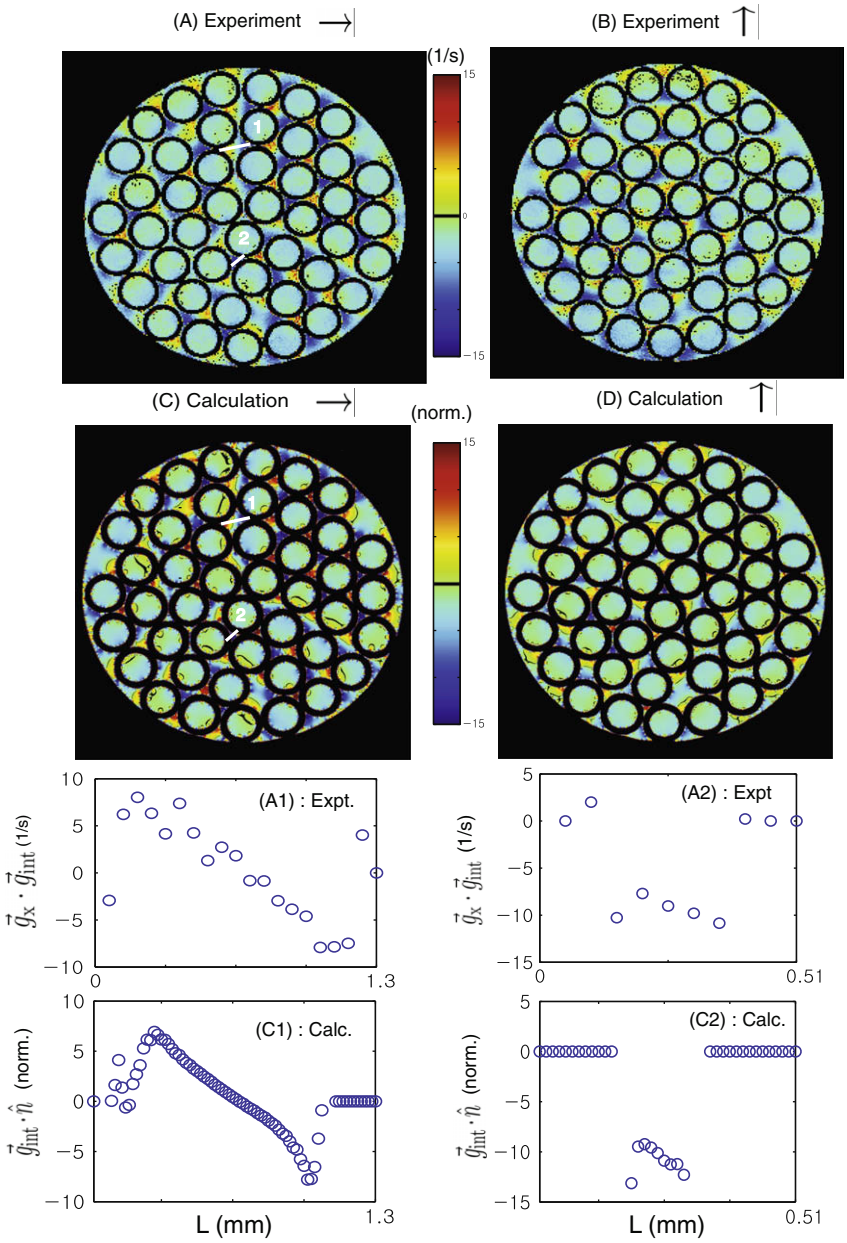

Fig. 5. Comparison of the experimental decay rates of the cross-terms between internal and external field gradients (A and B) and theoretical calculation of the angle-resolved internal gradients (C and D). (A1) and (A2) show measured decay rates of the cross-terms across the pores along the labeled crossing lines in (A), and (C1) and (C2) shows corresponding calculated angle-resolved internal gradient for the comparison. L is the coordinate along the lines. For comparison, the theoretical gradient value was multiplied by a factor in order to make it comparable to the experimental decay rate for the plots. $\hat{n}$ is the unit vector along the direction of applied external gradient. Note that the cylinder walls appear thicker in calculated images (1024×1024) because of interpolation step from lower resolution MR spin density image (256×256).

gular packing (A2 and C2), respectively. For comparison, the theoretical gradient value was multiplied by a factor in order to make it comparable to the experimental decay rate in the plots. The normalization factor was determined by comparing average value of internal gradients strength in pores of triangular packing between calculated and experimental values. The change of the direction of internal gradient across rectangular packing and negative (opposite to the direction of applied external gradient)uniform internal gradients were both reproduced with theoretical calculation of angle-resolved internal gradients. We also noted that the cylinder walls appear thicker in calculated images (1024×1024) because of the interpolation step from lower resolution MR spin density image (256×256), which leads to the slightly narrower pore length in triangular packing as shown in (A2) and (C2).

Measuring the interference patterns between external and internal gradients may be useful in determining the directionality of cylindrical objects, such as capillary blood vessels in tumors with blood-pool contrast agents [29]. Highly tortuous tumor vasculature is one of the characteristics of tumor angiogenesis and the ability to obtain a tortuosity index will provide important prognostic information. For example, a number of experiments with non-collinear external gradient directions can be performed to obtain the directional dependence of cross-terms between internal (structure specific) and external (user controllable) gradients. Then, the axial direction of capillary vessel can be probed due to the absence of cross-terms along the axial direction of the vessel.

4. Conclusion

Experimental DDIF rates were shown to be directly proportional to the local gradient strength obtained from theoretical calculations in a 2D model system of uniform glass tubes. Spatially resolved interference patterns of decay rates between internal and external pulsed field gradients (PFG) along different orientations were also obtained and corresponding cross-terms were extracted with DDIF microimaging. This work demonstrates a simple yet representative case for visualizing the strength and orientation of local susceptibility induced magnetic field gradients in porous media.

Acknowledgments

We thank Dr. Lukasz Zielinski and Dr. Phillip Zhe Sun for stimulating discussions. We also thank Dr. George Dai for his technical support and Dr. Khushali Kotedia for proof reading the manuscript. This work is supported in part by the National Institutes of Health (EB003869).

References

[1] S.D. Senturia, J.D. Robinson, Nuclear spin-lattice relaxation of liquids confined in porous solids, SPE 10 (1970) 237.
[2] M.H. Cohen, K.S. Mendelson, Nuclear magnetic relaxation and the internal geometry of sedimentary rocks, J. Appl. Phys. 53 (1982) 1127.
[3] R.L. Kleinberg, Well Logging, Encyclopedia of Nuclear Magnetic Resonance, vol. 8, Wiley, New York, 1995. pp. 4960.
[4] P.P. Mitra, P.N. Sen, L.M. Schwartz, P.L. Doussal, Diffusion propagators as a probe of structure of porous media, Phys. Rev. Lett. 68 (1992) 3555.
[5] L.L. Latour, L.M. Li, C.H. Sotak, Improved PFG stimulated echo method for the measurement of diffusion in inhomogeneous field, J. Magn. Reson. 101 (1993) 72.
[6] D.G. Cory, A.N. Garroway, Measurement of translational displacement probabilities by NMR: an indication of compartmentation, Magn. Reson. Med. 14 (1990) 435.
[7] P.T. Callaghan, A. Coy, D. Macgowan, K.J. Packer, F.O. Zelay, Diffraction-like effects in NMR diffusion studies if fluids in porous solids, Nature 6326 (1991) 351.
[8] S. Ryu, Probing pores using elementary quantum mechanics, Magn. Reson. Imaging 19 (2001) 411.
[9] M.D. Hurlimann, Effective gradients in porous media due to susceptibility differences, J. Magn. Reson. 131 (1998) 232.
[10] L.J. Zielinski, Effect of internal gradients in the nuclear magnetic resonance measurement of the surface to volume ratio, J. Chem. Phys. 121 (2004) 352.
[11] W.D. William, E.F.W. Seymour, R.M. Cotts, A pulsed-gradient multiple spin-echo NMR techniques for measuring diffusion in the presence of background magnetic field gradients, J. Magn. Reson. 31 (1978) 271.
[12] G.H. Sorland, B.H. Hafskjold, O. Herstad, A stimulated echo method for diffusion measurements in heterogeneous media using pulsed field gradients, J. Magn. Reson. 124 (1997) 172.
[13] J.G. Seland, G.H. Sorland, K. Zick, B. Hafskjold, Diffusion measurements at long observation times in the presence of spatially variable internal magnetic field gradients, J. Magn. Reson. 146 (2000) 14.
[14] P.Z. Sun, J.G. Seland, D.G. Cory, Background gradient suppression in pulsed gradient stimulated echo measurements, J. Magn. Reson. 161 (2003) 168.
[15] Y.-Q. Song, S. Ryu, P.N. Sen, Determining multiple length scales in rocks, Nature 406 (2000) 178.
[16] Y.-Q. Song, Detection of the high eigenmodes of spin diffusion in porous media, Phys. Rev. Lett. 85 (2000) 3878–3881.
[17] Q. Chen, M. Gingras, B. Balcom, A magnetic resonance study of pore filling processes during spontaneous imbibition in berea sandstone, J. Chem. Phys. 119 (2003) 479–493.
[18] R.J.S. Brown, Distribution of fields from randomly placed dipoles: free-precession signal decay as a result of magnetic grains, Phys. Rev. 121 (1961) 1379.
[19] P.N. Sen, S. Axelrod, Inhomogeneity in local magnetic field due to susceptibility contrast, J. Appl. Phys. 86 (1999) 4548.
[20] B. Audoly, P.N. Sen, S. Ryu, Y.-Q. Song, Correlation functions for inhomogeneous magnetic field in random media with application to a dense pack of spheres, J. Magn. Reson. 164 (2003) 154.
[21] C.H. Arns, A comparison of pore size distributions derived by NMR and X-ray–CT techniques, Physica A 339 (2004) 159–165.
[22] S. Ogawa, T.M. Lee, A.R. Kay, D.W. Tank, Brain magnetic resonance imaging with contrast dependent on blood oxygenation, Proc. Natl. Acad. Sci. 87 (1990) 9868–9872.
[23] S.N. Hwang, F.W. Wehrli, Experimental evaluation of a surface charge method for computing the induced magnetic field in trabecular bone, J. Magn. Reson. 139 (1999) 35–45.
[24] E.E. Sigmund, H. Cho, S. Byrnes, P. Chen, Y.-Q. Song, E.X. Guo, T. Brown, Diffusion based MR-method for bone structure and evolution, Magn. Reson. Med. 59 (2008) 28–39.
[25] D.C. Ailion, T.A. Case, D.D. Blatter, A.H. Morris, A.G. Cutillo, C.H. Durney, S.A. Johnson, Application of NMR spin imaging to the study of lungs, Bull. Magn. Reson. 6 (1984) 130–141.
[26] M. Salerno, J.R. Brookeman, E.E. de Lange, J.P. Mugler, Hyperpolarized ^{3}He lung imaging at 0.5 and 1.5 tesla: a study of susceptibility-induced effects, Magn. Reson. Med. 53 (2005) 212–216.
[27] S. Su, J.K. Saunders, I.C.P. Smith, Resolving anatomical details in lung parenchyma: theory and experiment for a structurally and magnetically inhomogeneous lung imaging model, Magn. Reson. Med. 33 (1995) 760–765.
[28] A.P. Pathak, B.D. Ward, K.M. Schmainda, A novel technique modelling susceptibility-based contrast mechanisms for arbitrary microvascular geometries: the finite perturber method, Neuroimage 40 (2008) 1130–1143.
[29] A. Vignaud, I. Rodriguez, D.B. Ennis, R. Desilva, P. Kellman, J. Taylor, E. Bennett, H. Wen, Detection of myocardial capillary orientation with intravascular iron-oxide nano particles in spin echo MRI, Magn. Reson. Med. 55 (2006) 725–730.
[30] L.-S. Bouchard, W.S. Warren, Reconstruction of porous material geometry by stochastic optimization based on bulk NMR measurements of the dipolar field, J. Magn. Reson. 170 (2) (2004) 299–309.
[31] G. Deville, M. Bernier, J.M. Delrieux, NMR multiple echoes observed in solid ^{3}He, Phys. Rev. B 19 (11) (1979) 5666.